

The variability of Antarctic ice-sheet response to the climatic signal

Frank PATTYN*

*Department of Geography, Vrije Universiteit Brussel, Pleinlaan 2, B-1050 Brussel, Belgium

Annals of Glaciology 29: 273-278

Abstract

High-resolution numerical model experiments were carried out along two flowlines in Dronning Maud Land (Antarctica), one flowline passing through the central part of a coastal mountain range and one along a major continental ice stream (Shirase Glacier). Results showed that ice-sheet behaviour in response to the climatic signal locally differs. Response patterns are different for the inland ice sheet, the coastal ice sheet and around marginal (subglacial) mountains. Modelled response time series were analyzed by lag-correlation, range and fractal analysis. Local differentiation in ice-sheet response is primarily related to the sensitive interplay between surface accumulation patterns, thermomechanical properties of the ice sheet and bedrock roughness.

Introduction

The East Antarctic ice sheet appears as a stable and dominant feature on earth at least for the last few million years. Three-dimensional model experiments (Huybrechts, 1993) demonstrated that a large temperature rise is necessary (more than

15 K) to reduce the ice sheet significantly. The reason why the East Antarctic ice sheet is able to resist a much larger warming than its West Antarctic counterpart is partly due to the presence of several mountain systems, enabling the ice sheet to retreat at a higher, hence colder, elevation if a significant warming would occur (Huybrechts, 1993). The three major systems are the Transantarctic Mountains, the Gamburtsev subglacial mountains in the central part of the East Antarctic craton and a semi-continuous belt of coastal mountains in Dronning Maud Land stretching from Heimefrontfjella in the west (15°W) to the Yamato Mountains in the east (35°E). These mountain systems are separated by large subglacial depressions, such as the Pensacola, Wilkes and Aurora subglacial basins between the Transantarctic and Gamburtsev Mountains, and Lambert Glacier between Gamburtsev subglacial mountains and Enderby Land. Within the Dronning Maud Land coastal mountain chain some transverse gaps are noticed, such as Jutulstraumen in the west and Shirase Glacier in the east, which together with Lambert Glacier form the most prominent continental ice streams of East Antarctica.

The alternation of marginal mountain glacier systems and fast-flowing continental ice streams imply a local differentiation in ice-sheet behaviour as a reaction to a changing climate, which is confirmed by observations. Stake measurements in Shirase Drainage Basin, Dronning Maud Land (Nishio and others, 1989; Toh and Shibuya, 1992) show a marked thinning rate of the ice sheet of more than one meter per year. However, in the nearby Sør Rondane Mountains, Moriwaki and others (1992) found that the maximum ice surface attained over the last 100,000 year was only a few meters higher than the present surface, whereby the authors concluded that only minor glacier fluctuations occurred over this period (in the order of a few meters to a few tens of meters). The first observation points to a dynamical ice sheet, while the second observation – made in a neighbouring area 500 km to the west – corroborates the idea of a very stable ice sheet. Also a different pattern in ice-sheet behaviour is observed between the coastal area and the inland ice sheet. While near the coast the Last Glacial Maximum (LGM) ice sheet is generally believed to be thicker, the LGM ice sheet is presumed to be thinner for central parts of Antarctica (Lorius and others, 1984; Jouzel and others, 1989).

In order to interpret the variety of observations with respect to present and past ice-sheet dynamics Pattyn (1996) proposed a numerical model experiment that could explain the present dynamics of fast-flowing glaciers. In a subsequent paper, Pattyn and Deleir (1998) presented an experimental framework to determine in a consistent way past glacier variations in a marginal mountain range by linking the climatic signal to the proxy record of glacial-geological observations through numerical ice-sheet modelling. In this paper, the result of both studies will be further analyzed. More details on the numerical model itself, can be found in those two publications.

Experimental setup

The numerical model is a time-dependent flowline model that predicts the ice thickness distribution along a fixed flowline in response to environmental conditions, according to

$$\frac{\partial H}{\partial t} = -\nabla \cdot (\vec{v}H) + M - S \quad (1)$$

where \vec{v} is the depth-averaged horizontal velocity, H the ice thickness, and M and S the surface mass balance and basal melting, respectively. The ice-sheet response $\frac{\partial H}{\partial t}$ is obtained by calculating at a given moment the two-dimensional flow regime (velocity, strain-rates and stress fields) and the temperature distribution, determined by the ice-sheet geometry and boundary conditions, on a numerical grid using finite differences. The main boundary conditions to the ice-flow field are the mass balance distribution at the surface, basal motion at the bottom an ice shelf at the outer edge. The temperature field is conditioned by surface temperature at the top and geothermal heat flux at the bottom. Additional sub-models entering as boundary conditions to the main system are considered as well, i.e. isostatic adjustment and heat conduction in the bedrock.

In this study numerical flowline modelling experiments will be carried out along two flowlines in Dronning Maud Land (Fig. 1), i.e. a flowline along a major ice stream (Shirase Drainage Basin: Shirase flowline, Fig. 2), and one flowline through the

central part of a coastal mountain range (Sør Rondane Mountains: Asuka flowline, Fig. 3). Both start at the Dome Fuji ice divide and reach beyond the edge of the continental plateau in the Southern Ocean.

Each model experiment is a twofold process. First, a steady-state ice sheet at 200 000 BP is established starting from an ice-free bedrock topography isostatically adjusted to the removal of the present ice load, under climatic conditions taken as the mean of the last 200 ka, i.e. a background temperature of -5.2 K compared to present. Second, the model is run forward in time, forced by the Vostok signal (Jouzel and others, 1993). Changes in surface temperature also affect accumulation rates, according to Lorius and others (1985):

$$M(t) = M(0) \exp \left[22.47 \left(\frac{T_0}{T_f(0)} - \frac{T_0}{T_f(t)} \right) \right] \left[\frac{T_f(0)}{T_f(t)} \right]^2 \quad (2)$$

where M is the surface accumulation rate (m a^{-1}), $T_0 = 273.15 \text{ K}$, $T_f(t) = 0.67T_s(t) + 88.9$ the temperature above the inversion layer (Jouzel and Merlivat, 1984) and $T_s(t)$ the surface temperature. This means that changes in surface accumulation rate exactly follow changes in background temperature. Thus, for each gridpoint along the flowline a local time series according to Eq. 2 and a local ice-sheet response time series according to Eq. 1 of vertical ice-surface changes over the last 200 000 years is obtained.

The Shirase flowline experiments

Previous modelling experiments of Shirase Glacier (Pattyn and Declair, 1995) showed that the large observed thinning rate could not be explained as a reaction to the climate signal alone. Another mechanism should account for this. A new model formulation – taking into account the physical properties of ice streams, i.e. longitudinal stresses in the force budget and different basal motion models (Pattyn, 1996) – revealed different patterns of cyclic behaviour in ice streams depending on the basal boundary conditions. In this study similar experiments are repeated, this

time applied to the Shirase flowline. Basal motion was treated by considering a water film underneath the ice sheet, as radio-echo sounding measurements (Nishio and Uratsuka, 1991) demonstrated that subglacial water is omnipresent in the downstream area of the Shirase drainage basin. According to Weertman and Birchfield (1982), the sliding velocity is dependent on the depth of the water layer δ and the critical particle size δ_c

$$\begin{aligned} u_s &= A_s \tau_b^p \left(1 + 10 \frac{\delta}{\delta_c} \right) & \text{if } \delta < \delta_c \\ &= 10 A_s \tau_b^p \frac{\delta}{\delta_c} & \text{if } \delta \geq \delta_c \end{aligned} \quad (3)$$

and

$$\delta = \left(\frac{12 \mu Q_w}{P_g} \right)^{\frac{1}{3}} \quad (4)$$

where Q_w is the water flux per unit width (m^2s^{-1}), calculated through downstream integration of the basal melting rate, and P_g the pressure gradient (Alley, 1989). A_s is a sliding law constant (taken as $2.0 \cdot 10^{-11} \text{ Pa}^{-2} \text{ m}^{-1} \text{ a}^{-1}$) and τ_b the shear stress at the base of the ice sheet. Two model experiments were carried out, both over a period of 200 000 year forced by the Vostok signal: the first model run (TYPE I) based on the sliding law of Eq. 3; the second (TYPE II) based on a Weertman sliding law which is independent of the presence of subglacial water and widely used in numerical ice-sheet modelling (Fig. 4). According to the TYPE I experiment, high frequency oscillations occur during the coldest phase of the glacial periods and during the warmest phase of the interglacials. As explained in Pattyn (1996) they are due to the interaction of the ice-sheet temperature field and the conditions at the base: basal motion causes the ice sheet to move more rapidly, hence increasing horizontal and vertical advection rates. Cold ice is thus advected towards the bottom, hence reducing the total surface subjected to melting. Basal velocities decrease, stabilizing the ice-sheet motion. The whole process gives rise to a cyclic behaviour; the slower ice sheet will tend to grow, advection rates decrease, bottom melting increases, hence resulting in large basal velocities. The periodicity of these cycles is approximately 3000 to 4000 years. High frequency oscillations are only observed in the downstream

area of Shirase Glacier, and disappear gradually towards the inland plateau (Fig. 5).

Payne (1995) showed a similar cyclic behaviour with a thermomechanical ice-sheet model, including a basal sliding mechanism according to TYPE II. His model produced limit cycles that are caused by on-and-off switching of sliding as basal ice reaches the pressure melting point. Our TYPE II experiments do not show any cyclic behaviour for a sliding law in which the effect of basal water is not explicitly included, due to a lower tuning value compared to the sliding law of Payne (1995) and the fact that sliding is also made possible when basal temperatures are lower than the pressure-melting point, thus avoiding abrupt on and off switching between sliding / no sliding conditions.

The TYPE I experiments show that there is no need for a massive drainage in the coastal area of Shirase Glacier to explain the large thinning rate observed in the field, the high frequency of the oscillations account for this, while the ice sheet remains stable. Any runaway of ice is counteracted by the thermomechanical process described above. A marine instability is unlikely to occur since most of the bedrock lies above sea level.

The Asuka flowline experiments

Using an experimental framework, Pattyn and Declerq (1998) carried out a large number of model experiments each with different settings of boundary conditions. The results were then compared with glacial-geological evidence and field measurements such as ice velocities and ice thickness. Experiments in agreement with these observations could be divided in two major groups or scenarios. The first scenario (T-COUPLING) is the so-called standard model experiment, i.e. with full thermomechanical coupling (ice stiffness depends on local ice temperature), while for the second scenario (ISOTHERM) a constant flow parameter for the whole ice sheet is used, i.e. independent of the ice-temperature distribution (constant ice stiffness). Although the response time series of both scenarios are similar along the flowline, a marked discrepancy is observed in the mountain area (Fig. 4). One interpretation

(T-COUPPING) is that only minor glacier variations have occurred during the last 200 ka, as was concluded by Moriwaki and others (1992) based on glacial-geological evidence, and the present glacier surface is close to its minimum, while the other interpretation (ISOTHERM) is that glacier variations are of the order of 60 m, but that the present glacier surface is close to its maximum elevation of the last 200 ka. Outside the Sør Rondane (not shown), on the polar plateau, as well as in the coastal area, both scenarios are in accord and ice-sheet surface variations are of the order of 60-80 m. The main difference between the inland area and the coast is that near the ice divide the ice sheet seems at present close to its maximum position, while in the coastal area deglaciation is completed and the ice-sheet surface seems close to its minimum.

Analysis of time series

The model ice sheet reacts to the climatic signal according to Eq. 1, where the rate of change of the ice sheet $\frac{\partial H}{\partial t}$ is a function of changes in the surface mass balance (through $M(x, t)$) and a function of changes in ice temperature (that influence the velocity field and hence the flux-divergence term in Eq. 1). The complexity and non-linear nature of this relation make that $H(x, t)$ will differ from the climatic record that enters the model as $M(x, t)$ and $T_s(x, t)$. One way to investigate the response of the ice sheet to changes in climate is by comparing the time series of $H(x, t)$ and $M(x, t)$ in both time and spectral domain.

Lag correlation analysis

The reaction time of the ice sheet to the climatic signal can be expressed by the time lag. The correlation between the forcing time series (surface accumulation rate at a given gridpoint $M(x, t)$) and the response time series (ice-surface variations at that gridpoint $H(x, t)$) was calculated for different lags using the fast Fourier transform (Press and others, 1992). The lag corresponding to the maximum correlation then gives the time lag between both time series (Fig. 6). For all model experiments,

the time lag is positive for the interior ice sheet and gradually decreases towards the coast, meaning that a maximum ice-surface elevation is reached some time (2-5 ka) *after* the maximum of the accumulation rate signal. However, the T-COUPPING experiment shows a large negative time lag clearly associated with the presence of the mountain range. The ISOTHERM experiment does not show this discrepancy, hence the negative time lag is probably due to differences in ice stiffness along the flowline as basal temperatures are low in the mountain area and increase rapidly northward of the ice fall (Fig. 3). This feature is also present in the graph of the maximum correlation that corresponds to the time lag (Fig. 7), implying that in areas characterized by a negative time lag, the shape of the response signal might differ slightly from the input signal as correlation coefficients are rather low.

A slight negative time lag is also observed for the TYPE I experiment along the Shirase flowline. Although a damming mountain range is not present in this area, a subglacial continuation of the mountain chain can be observed between 400 and 600 km from the ice divide, associated with a similar pattern in the basal temperature profile (Fig. 2).

Range analysis

The amplitude of the response time series, i.e. the range of vertical surface variations at each gridpoint, is taken as the difference between the maximum and the minimum of the series (Fig. 8). Generally, the range of ice-surface variations along the Shirase flowline is higher (150-200 m) than for the Asuka experiments (40-100 m). Since ice thickness in the inland part are comparable for both flowlines, the difference might be due to a lower accumulation rate in the Asuka drainage basin. Furthermore, ice motion is much faster in the Shirase drainage basin. Again, all four curves in Fig. 8 display a marked jump associated with the presence of the (subglacial) mountain range. The lowest amplitude is encountered in the mountain area for the T-COUPPING experiment, which corresponds to the time series of Fig. 4.

Fractal analysis

Long-term climatic series are considered to be self-affine (non-isotropic) fractals (Fluegelman and Snow, 1989; Turcotte, 1992), characterized by a fractal dimension lying between 1.0 and 1.5. A fractal analysis of the oxygen isotope record of the Pacific Core V28-293 revealed a fractal dimension of 1.22, meaning that such time series shows persistence through time (Fluegelman and Snow, 1989). The aim of this study is to use a fractal analysis – or an analysis of variance on different time scales – to interpret the difference in response patterns along the two flowlines. A common technique is the rescaled range analysis (RSA; Feder, 1988) that was applied to the the time series of local imbalance $\xi(t) = \frac{\partial H}{\partial t}$. The rescaled range R/S then is the ratio of the range R , i.e. the difference between the maximum and minimum of cumulated values of ξ at time t over a time span τ , and the standard deviation S estimated from the observed values $\xi(t)$

$$\begin{aligned}
 R(\tau) &= \max_{1 \leq t \leq \tau} X(t, \tau) - \min_{1 \leq t \leq \tau} X(t, \tau), \\
 S(\tau) &= \left(\frac{1}{\tau} \sum_{u=1}^{\tau} (\xi(u) - \langle \xi \rangle_{\tau})^2 \right)^{\frac{1}{2}}, \quad \text{where} \\
 X(t, \tau) &= \sum_{u=1}^t (\xi(u) - \langle \xi \rangle_{\tau}), \\
 \langle \xi \rangle_{\tau} &= \frac{1}{\tau} \sum_{t=1}^{\tau} \xi(t)
 \end{aligned} \tag{5}$$

The rescaled range is shown to have a power law dependence on time span τ (Feder, 1988)

$$R/S \sim \tau^H \tag{6}$$

where H is the Hurst exponent. If H is greater than 0.5 and less than 1.0, it is related to the fractal dimension by $D_H = 2 - H$ (Fluegelman and Snow, 1989). For each response time series along the flowline D_H was determined from a linear least squares fit of $\log(R/S)$ versus $\log(\tau)$ (Fig. 9 and 10). For the Asuka flowline

experiments D_H lies between 1.1 and 1.3, gradually increasing towards the coast. A small bump is observed near the mountain area for the T-COUPPING as well as for the ISOTHERM experiment, although the D_H of the latter is lower over the whole flowline. A much higher fractal dimension is observed for the TYPE I experiment associated with the occurrence of the high frequency oscillations, which is not shown in the TYPE II experiment. The sharp vertical jump in this D_H curve around 600 km from the ice divide (Fig. 10) marks the limit of the influence area of these oscillations.

The variance on different time spans of the response signal increases towards the coast, but is hardly influenced by the presence of subglacial mountains, nor the contrast in stiffer / softer ice. Different response patterns in terms of high frequency oscillations account for a high fractal dimension. With exception of the TYPE I experiment, the fractal dimension of the response series is lower than the D_H of the input signal (taken as $\xi = \frac{\partial M}{\partial t}$). This means that the response signals are smoother and that small scale climatic variations have less effect on the ice-sheet response.

Discussion and conclusions

Numerical ice-sheet model experiments were capable of simulating different response patterns of the East Antarctic ice sheet to the climatic signal as observed in the field, i.e. the large thinning rate in Shirase drainage basin and the small glacier variations that – according to glacial-geological evidence – occurred over the last 200 ka in the nearby Sør Rondane Mountains, Dronning Maud Land. Whether the high frequency oscillations, as a result of the interaction between the ice-sheet thermodynamics and basal sliding, are a dynamic process that really occurs in Shirase drainage basin has never been proven due to the lack of field evidence. However, similar mechanisms are capable of explaining the dynamics of the Siple Coast ice streams, i.e. a switching between fast and slow ice-stream flow (Payne, 1998).

All of the above described time series analyses, i.e. lag correlation, range and fractal analysis, demonstrate that the presence of a coastal mountain range influences to a large extent the response of the ice sheet to the climatic signal, not only in places

where the ice is clearly dammed (Sør Rondane for instance), but also where a subglacial continuation of this mountain chain is visible (Shirase Glacier). In the first case (Asuka flowline) the damming effect is observed by the marked concavity in the ice-surface topography forming an ice fall (Fig. 3, upper panel) and the reduced surface velocities at the bottom of the ice fall (compressed flow), while in the latter case (Shirase flowline) none of these are observed. The lag correlation analysis in particular reveals something more: in the case of the Asuka flowline experiments, the time lagged response of the ice sheet is positive along the whole flowline when an isotherm ice sheet is considered (ISOTHERM). However, a marked differentiation is observed when full thermomechanical coupling is considered (T-COUPLING). Since most of the ice deformation is concentrated in the lower (basal) layers of the ice sheet, basal temperature controls to a large extent the flow characteristics of the ice sheet. For both flowlines, cold basal temperatures are found in the presence of subglacial mountains (Figs. 2 and 3, lower panel), where a small ice thickness and a high surface elevation imply a faster advection of cold ice towards the base of the ice sheet.

While both lag-correlation and range analysis clearly show an aberrant ice-sheet behaviour related to the presence of subglacial mountains, the fractal analysis only accounts for the effect of coastal high frequency oscillations caused by basal sliding. The fractal dimension of the ice-sheet response is lower than the dimension of the input signal, but increases towards the coast, hence the ice-sheet response is smoother in the interior than in the coastal area.

Acknowledgements

This paper forms a contribution to the Belgian Research Programme on the Antarctic (Federal Office for Scientific, Technical and Cultural Affairs), contract A4/DD/E03. I should like to thank G. Boulton and R. Greve for reviewing this paper.

References

- Alley, R. 1989. Water-pressure coupling of sliding and bed deformation: I. water system. *J. Glaciol.*, **35**(119), 108–118.
- Feder, J. 1988. *Fractals*. Plenum Press (New York).
- Fluegelman, R. H., and R. S. Snow. 1989. Fractal analysis of long-range paleoclimatic data: Oxygen isotope record of Pacific Core V28-239. *Pure and Applied Geophysics (PAGEOPH)*, **131**(1/2), 307–313.
- Huybrechts, P. 1993. Glaciological modelling of the Late Cenozoic East Antarctic ice sheet: Stability or dynamism? *Geografiska Annaler*, **75A**(4), 221–238.
- Jouzel, J., and others. 1993. Extending the Vostok ice-core record of palaeoclimate to the penultimate glacial period. *Nature*, **364**(6436), 407–411.
- Jouzel, J., and L. Merlivat. 1984. Deuterium and Oxygen 18 in precipitation: Modelling of the isotopic effects during snow formation. *J. Geophys. Res.*, **89**(D7), 11749–11757.
- Jouzel, J., G. Raisbeck, J. Benoist, F. Yiou, C. Lorius, D. Raynaud, J. Petit, N. Barkov, Y. Korotkevitch, and V. Kotlyakov. 1989. A comparison of deep Antarctic ice cores and their implication for climate between 65,000 and 15,000 years ago. *Quat. Res.*, **31**(2), 135–150.
- Lorius, C., J. Jouzel, C. Ritz, L. Merlivat, N. Barkov, Y. Korotkevich, and V. Kotlyakov. 1985. A 150,000-year climatic record from Antarctic ice. *Nature*, **316**(6029), 591–596.
- Lorius, C., D. Reynaud, J. Petit, J. Jouzel, and L. Merlivat. 1984. Late glacial maximum – Holocene atmospheric and ice-thickness changes from Antarctic ice-core studies. *Ann. Glaciol.*, **5**, 88–94.
- Moriwaki, K., K. Hirakawa, M. Hayashi, and S. Iwata. 1992. Late Cenozoic history in the Sør Rondane Mountains, East Antarctica. In Yoshida, Y., K. Kaminuma, and

- K. Shirashi, editors, *Recent Progress in Antarctic Earth Science*, pages 661–667. Tokyo, Terra Sci. Publ.
- Nishio, F., S. Mae, H. Ohmae, S. Takahashi, M. Nakawo, and K. Kawada. 1989. Dynamical behavior of the ice sheet in Mizuho Plateau, East Antarctica. *Proc. NIPR Symp. Polar Meteorol. Glaciol.*, **2**, 97–104.
- Nishio, F., and S. Uratsuka. 1991. Subglacial water layer and grounding line derived from backscattering coefficients of radio echo sounding in the Shirase Glacier and Roi Baudouin Ice Shelf, East Antarctica. *Proc. NIPR Symp. Polar Meteorol. Glaciol.*, **4**, 93–102.
- Pattyn, F. 1996. Numerical modelling of a fast-flowing outlet glacier: Experiments with different basal conditions. *Ann. Glaciol.*, **23**, 237–246.
- Pattyn, F., and H. Declair. 1995. Numerical simulation of Shirase Glacier, East Queen Maud Land, Antarctica. *Proc. NIPR Symp. Polar. Meteorol. Glaciol.*, **9**, 87–109.
- Pattyn, F., and H. Declair. 1998. Ice dynamics near Antarctic coastal mountain ranges: Implications for interpreting the glacial-geological evidence. *Ann. Glaciol.*, **27**, in press.
- Payne, A. 1995. Limit cycles in the basal thermal regime of ice sheets. *J. Geophys. Res.*, **100**(B3), 4249–4263.
- Payne, A. 1998. Dynamics of the Siple Coast ice streams, West Antarctica: results from a thermomechanical ice sheet model. *Geophys. Res. Letters*, **25**(16), 3173–3176.
- Press, W., S. Teukolsky, W. Vetterling, and B. Flannery. 1992. *Numerical Recipes in C: The Art of Scientific Computing*. Cambridge University Press (Cambridge), 2nd edition.
- Toh, H., and K. Shibuya. 1992. Thinning rate of ice sheet on Mizuho Plateau, East Antarctica, determined by GPS differential positioning. In Yoshida, Y.,

K. Kaminuma, and K. Shirashi, editors, *Recent Progress in Antarctic Earth Science*, pages 579–583. Tokyo, Terra Sci. Publ.

Turcotte, D. 1992. *Fractals and Chaos in Geology and Geophysics*. Cambridge, Cambridge University Press.

Weertman, J., and G. Birchfield. 1982. Subglacial water flow under ice streams and West Antarctic ice sheet stability. *Ann. Glaciol.*, **3**, 316–320.

List of Figures

1	<i>Situation map of Dronning Maud Land with the two modelled flowlines.</i>	17
2	<i>Present modelled longitudinal profile of the Shirase flowline after 200 ka of forward integration. Lower panel displays the corresponding basal temperature profile.</i>	18
3	<i>Present modelled longitudinal profile of the Asuka flowline after 200 ka of forward integration. Lower panel displays the corresponding basal temperature profile.</i>	19
4	<i>Time series of TYPE I (solid line) and II (dotted line) experiments along the Shirase flowline at gridpoint a (upper panel); time series of T-COUPPING (solid line) and ISOTHERM (dotted line) experiments along the Asuka flowline at gridpoint b (middle panel); time series of surface accumulation rate at gridpoint b. (see Fig. 1 for situation of points a and b along both flowlines)</i>	20
5	<i>Time-space map of vertical surface variations (compared to present) along the Shirase flowline for the TYPE I experiment.</i>	21
6	<i>Time lag between the input and response time series at each gridpoint along the flowline for the four experiments, i.e. TYPE I (open circle) and TYPE II (filled circle) along the Shirase flowline; T-COUPPING (open triangle) and ISOTHERM (filled triangle) along the Asuka flowline.</i>	22
7	<i>Maximum correlation coefficient corresponding to the time lag between the input and response time series at each gridpoint along the flowline for the four experiments. Same legend as Fig. 6.</i>	23
8	<i>Range (difference between maximum and minimum) of the vertical ice-surface variations at each gridpoint along the flowline for the four experiments. Same legend as Fig. 6.</i>	24

9	<i>Plot of $\log(R/S)$ versus $\log(\tau)$ for the time series according to the T-COUPPING experiment of the Asuka flowline at gridpoint b. The slope of the fitted line $H = 0.78$, representing a fractal dimension of $D_H = 1.22$.</i>	25
10	<i>Fractal dimension determined by rescaled range analysis of the variation of local imbalance at each gridpoint along the flowline for the four experiments. The dotted line shows the fractal dimension of the input signal $(\frac{\partial M}{\partial t})$ which is constant along the flowline. Same legend as Fig. 6.</i>	26

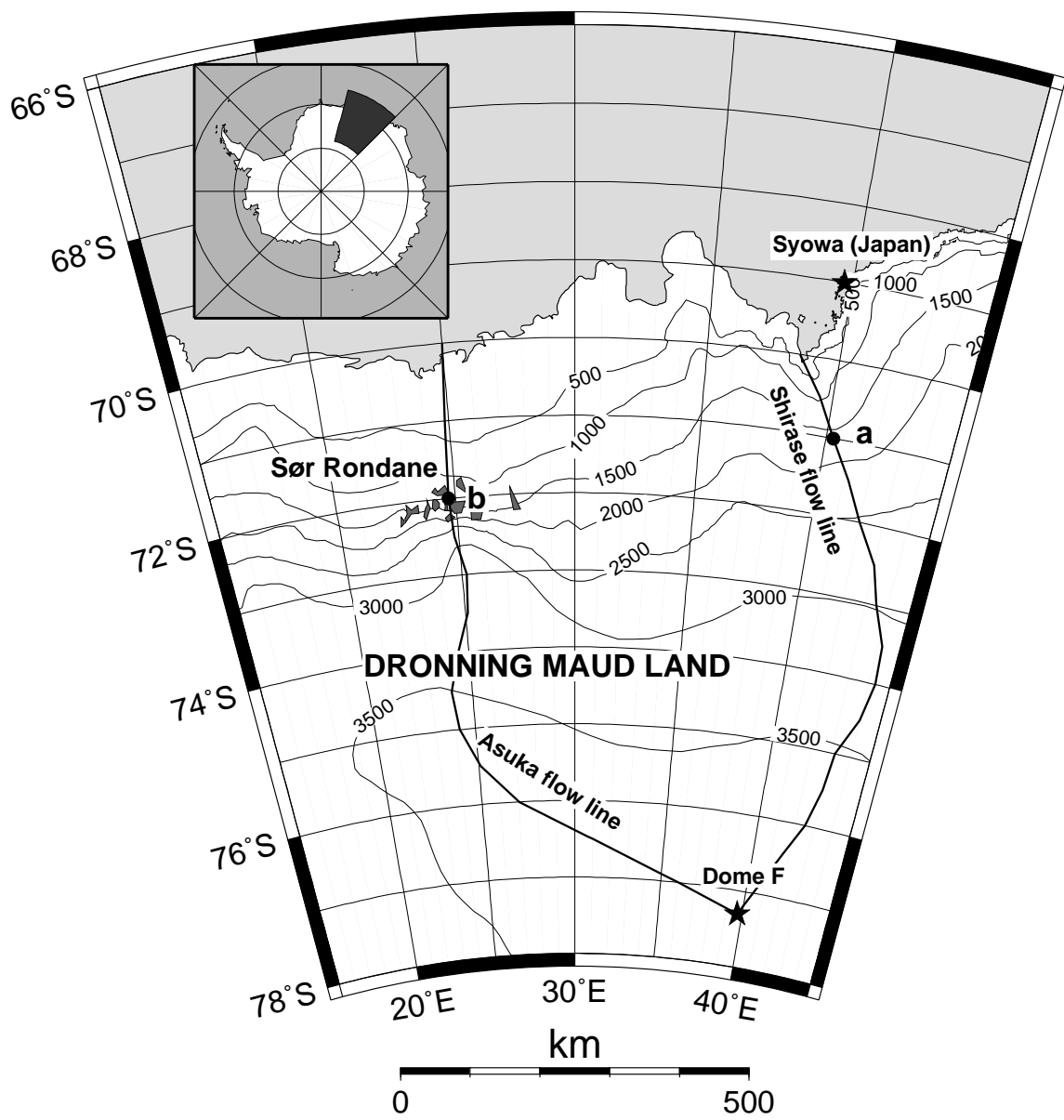


Figure 1: *Situation map of Dronning Maud Land with the two modelled flowlines.*

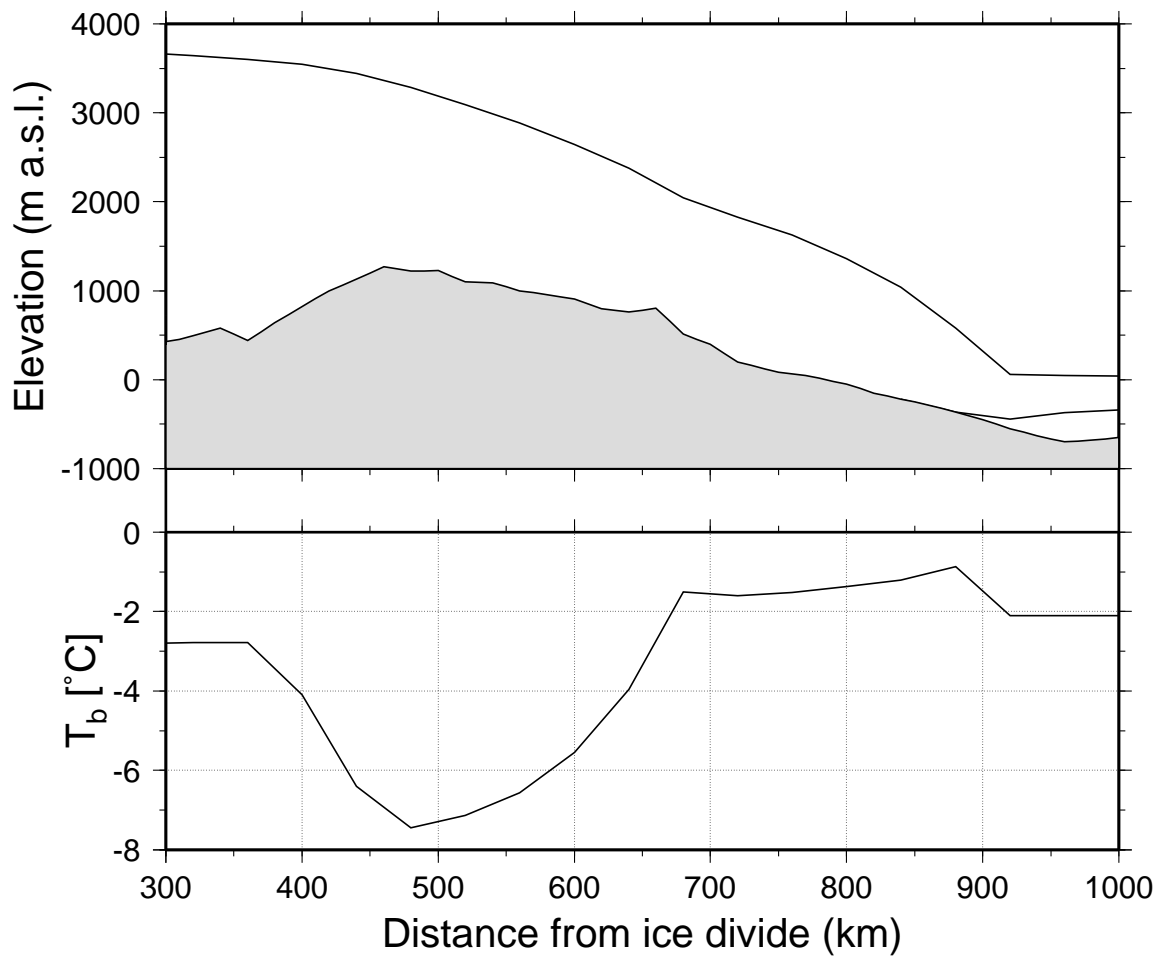


Figure 2: *Present modelled longitudinal profile of the Shirase flowline after 200 ka of forward integration. Lower panel displays the corresponding basal temperature profile.*

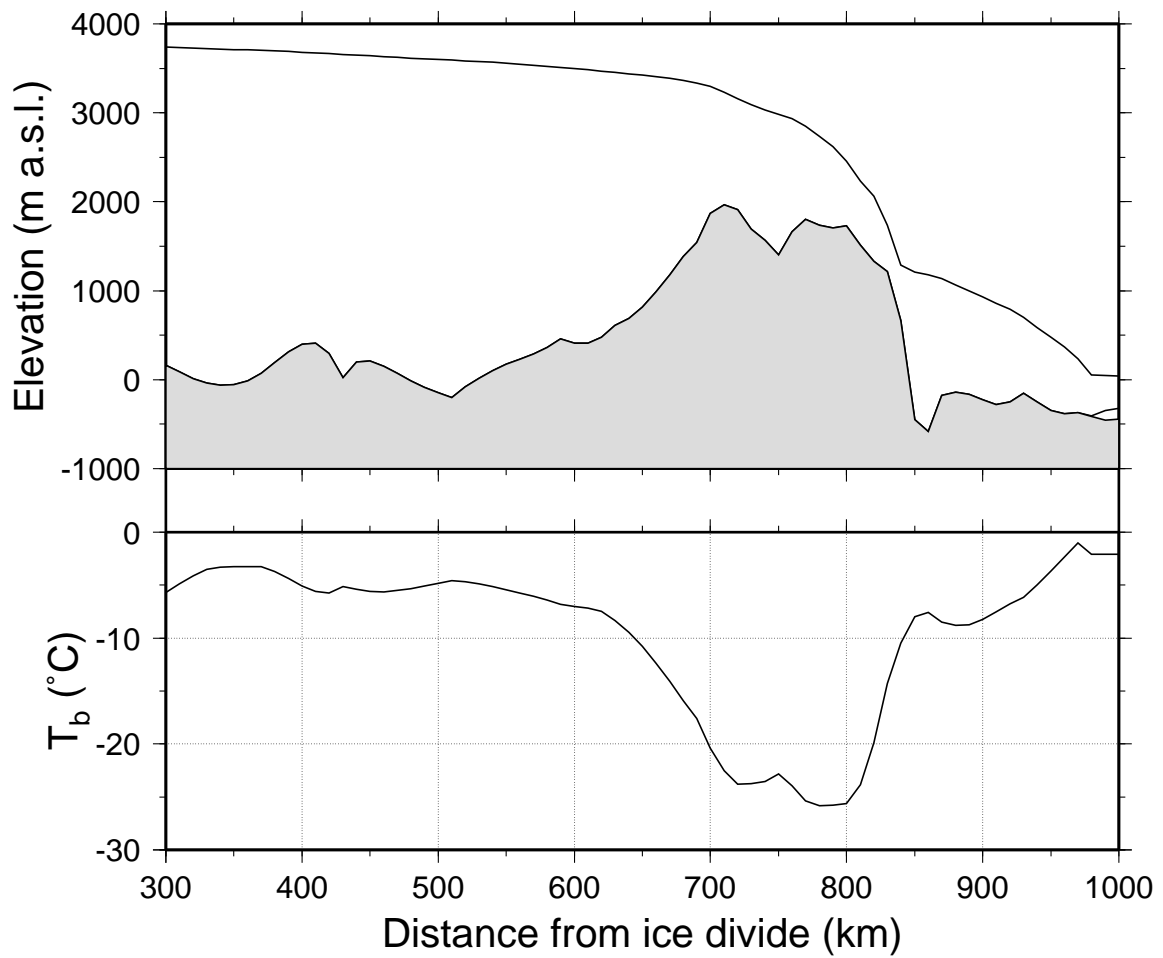


Figure 3: *Present modelled longitudinal profile of the Asuka flowline after 200 ka of forward integration. Lower panel displays the corresponding basal temperature profile.*

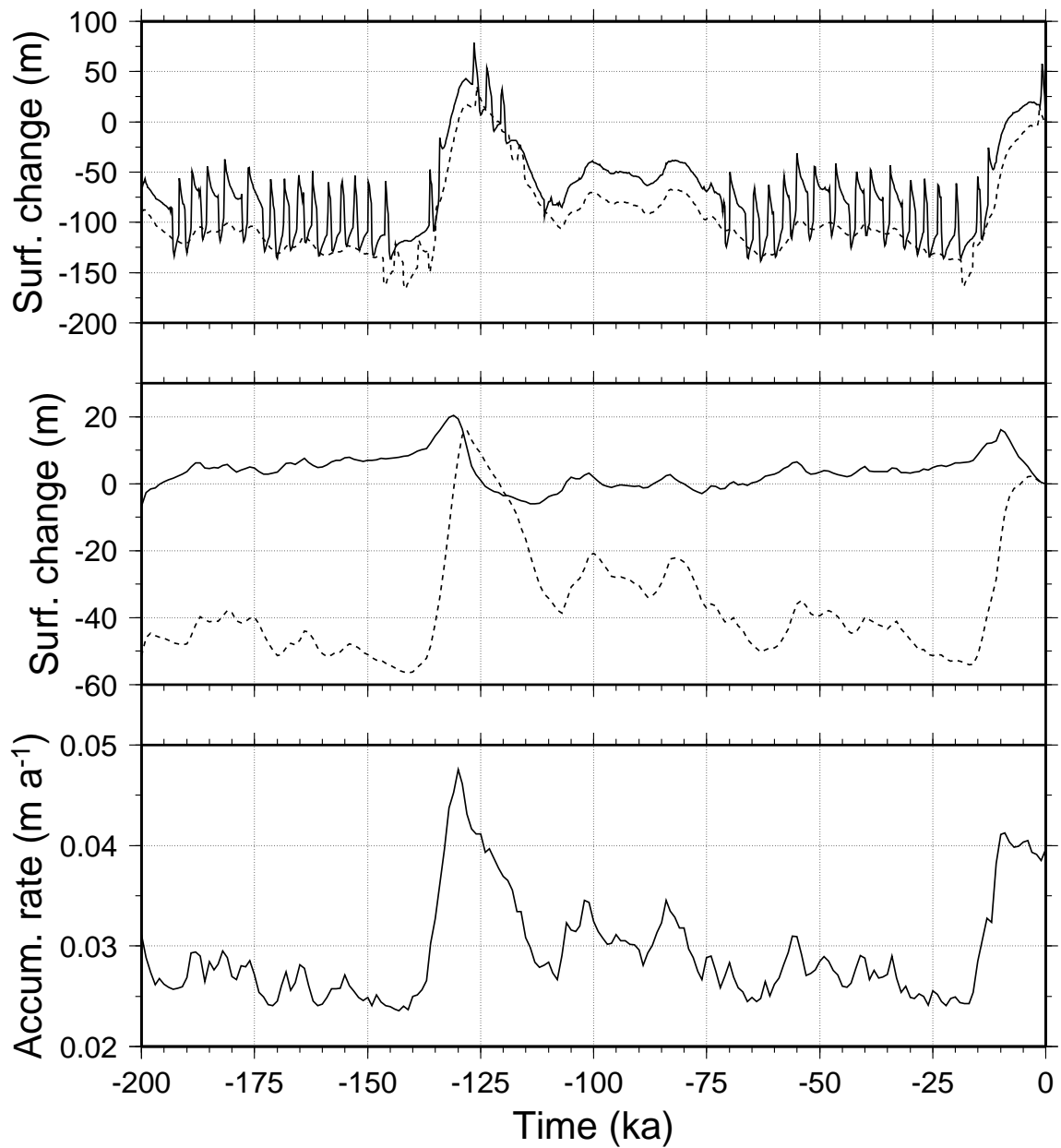


Figure 4: *Time series of TYPE I (solid line) and II (dotted line) experiments along the Shirase flowline at gridpoint a (upper panel); time series of T-COUPLING (solid line) and ISOTHERM (dotted line) experiments along the Asuka flowline at gridpoint b (middle panel); time series of surface accumulation rate at gridpoint b. (see Fig. 1 for situation of points a and b along both flowlines)*

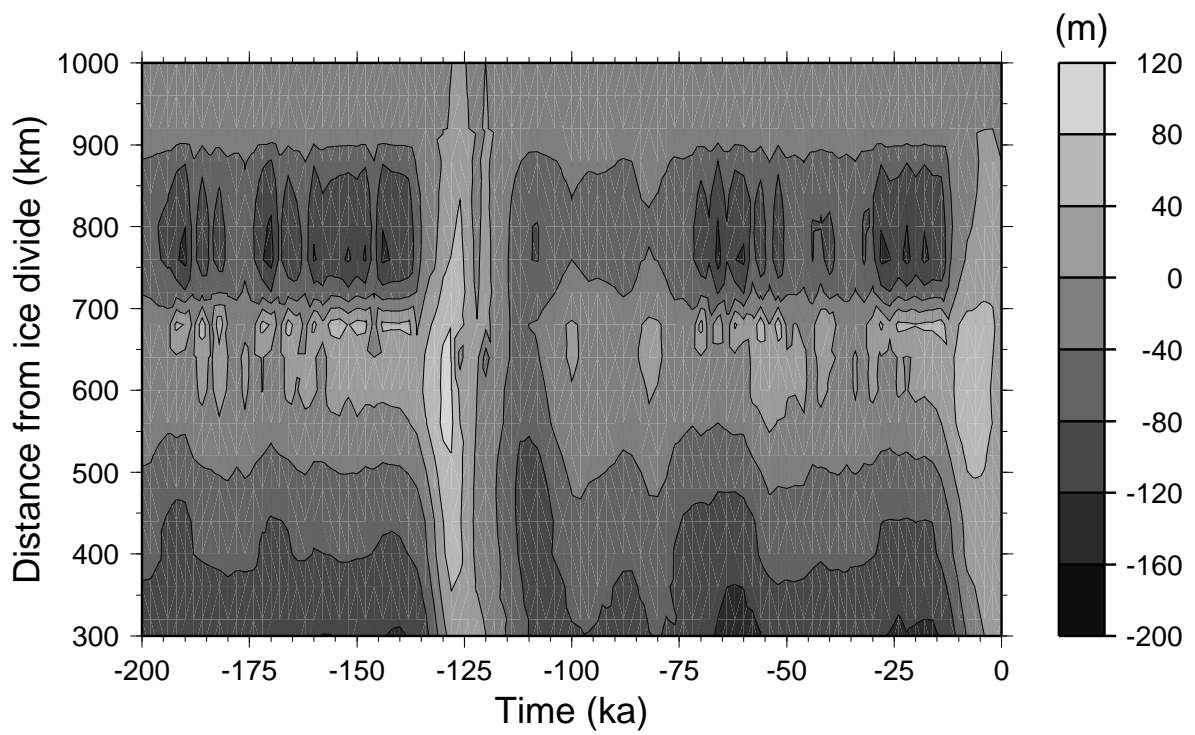


Figure 5: *Time-space map of vertical surface variations (compared to present) along the Shirase flowline for the TYPE I experiment.*

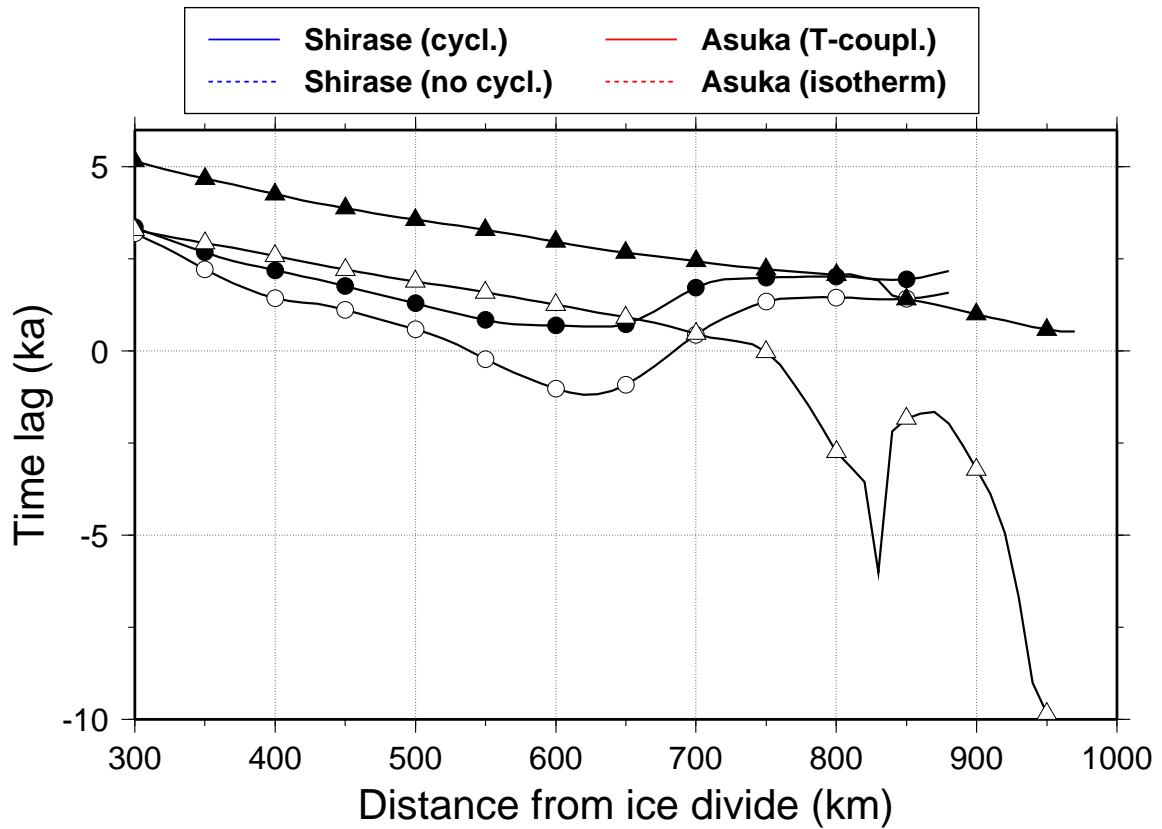


Figure 6: *Time lag between the input and response time series at each gridpoint along the flowline for the four experiments, i.e. TYPE I (open circle) and TYPE II (filled circle) along the Shirase flowline; T-COUPPING (open triangle) and ISOTHERM (filled triangle) along the Asuka flowline.*

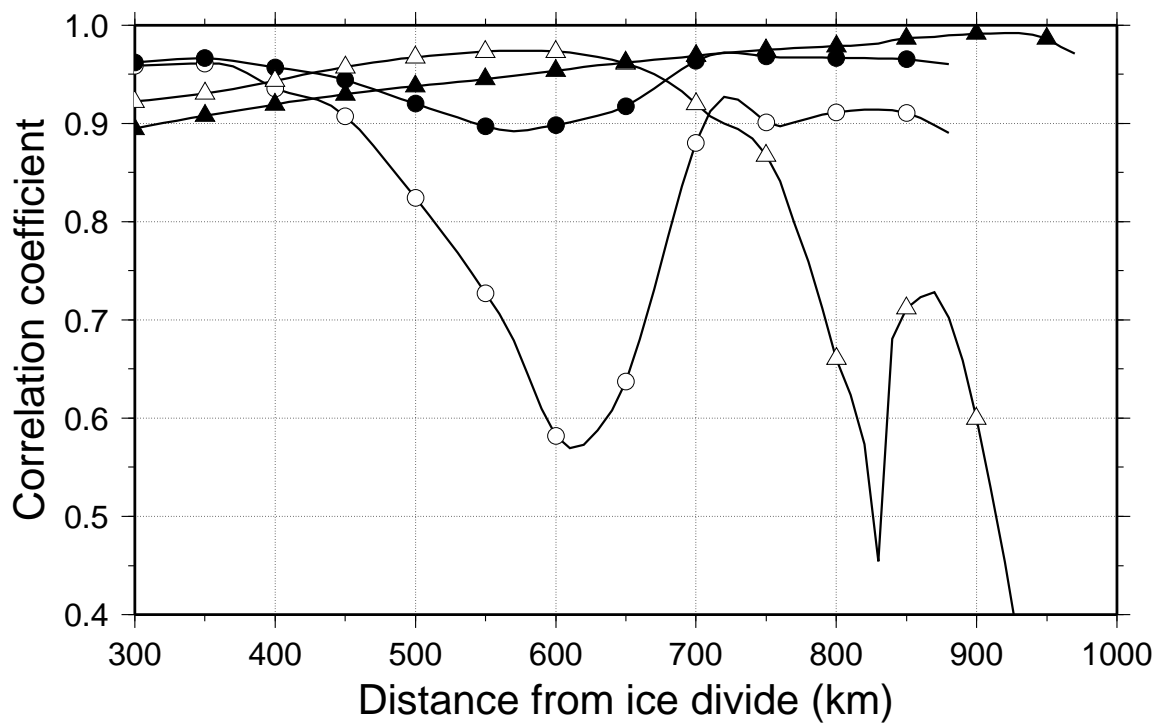


Figure 7: *Maximum correlation coefficient corresponding to the time lag between the input and response time series at each gridpoint along the flowline for the four experiments. Same legend as Fig. 6.*

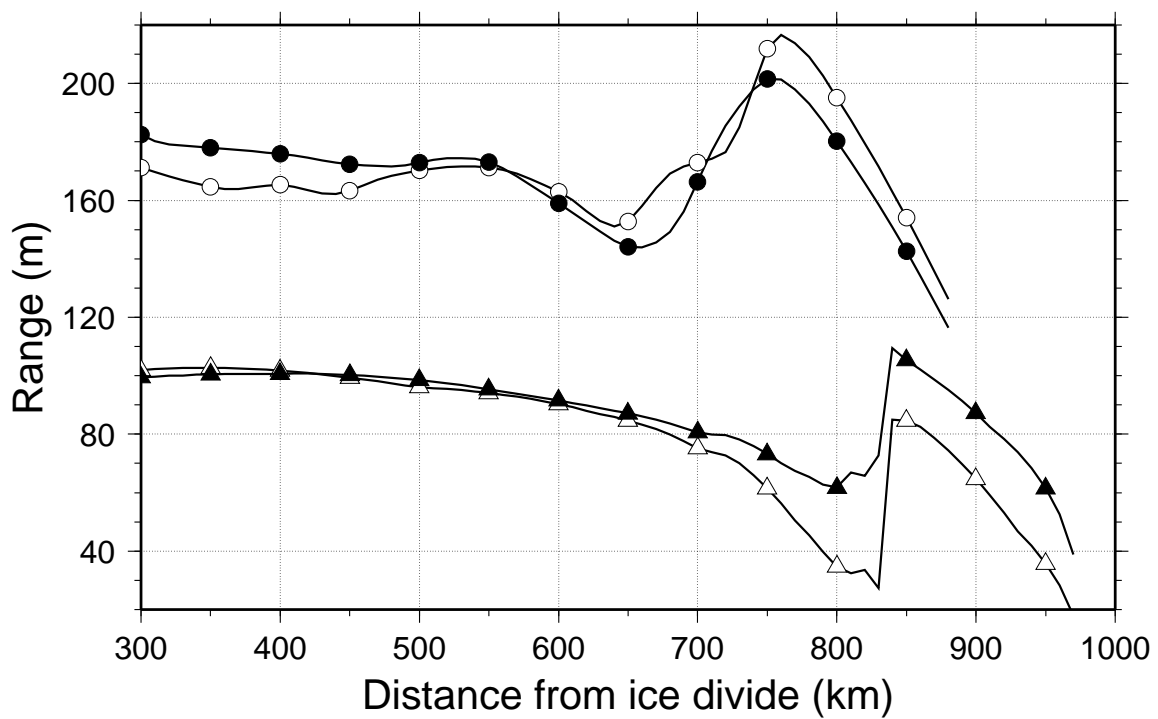


Figure 8: *Range (difference between maximum and minimum) of the vertical ice-surface variations at each gridpoint along the flowline for the four experiments. Same legend as Fig. 6.*

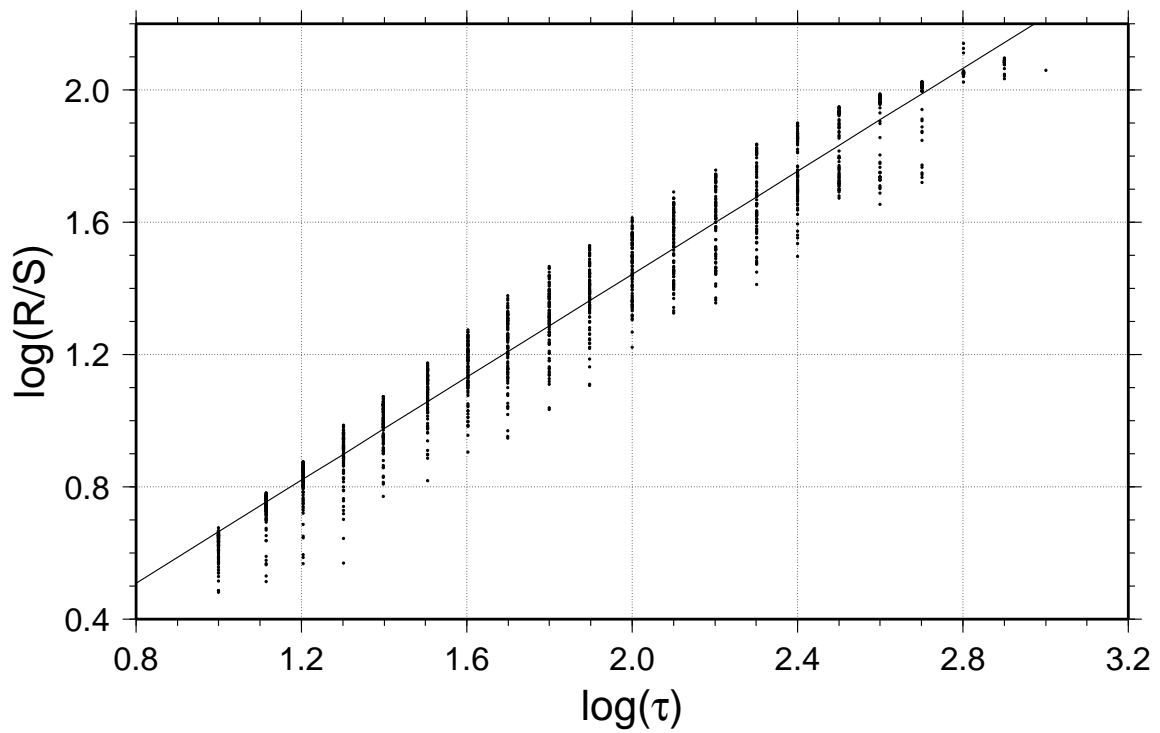


Figure 9: *Plot of $\log(R/S)$ versus $\log(\tau)$ for the time series according to the T-COUPLING experiment of the Asuka flowline at gridpoint b. The slope of the fitted line $H = 0.78$, representing a fractal dimension of $D_H = 1.22$.*

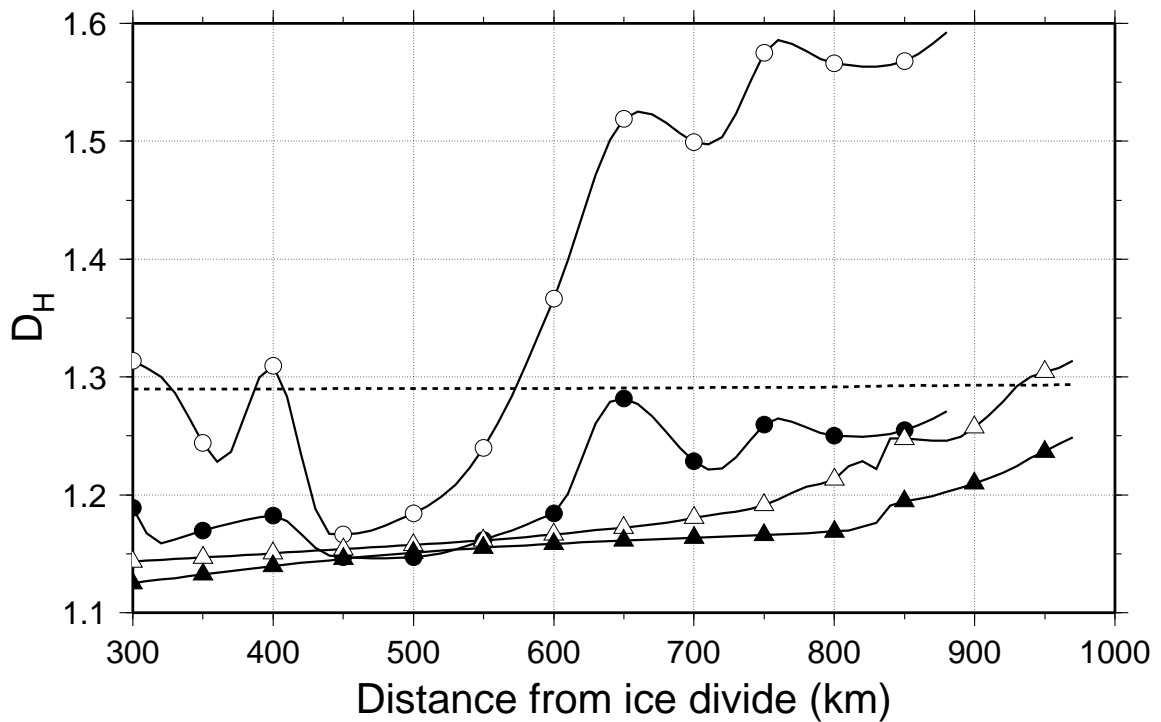


Figure 10: *Fractal dimension determined by rescaled range analysis of the variation of local imbalance at each gridpoint along the flowline for the four experiments. The dotted line shows the fractal dimension of the input signal ($\frac{\partial M}{\partial t}$) which is constant along the flowline. Same legend as Fig. 6.*